PixelGaussian: Generalizable 3D Gaussian Reconstruction from Arbitrary Views

Xin Fei[1,2,*]   **Wenzhao Zheng**[1,2,†]   **Yueqi Duan**[1]   **Wei Zhan**[2]
Masayoshi Tomizuka[2]   **Kurt Keutzer**[2]   **Jiwen Lu**[1]
[1]Tsinghua University   [2]University of California, Berkeley
feix21@mails.tsinghua.edu.cn; wenzhao.zheng@outlook.com
https://wzzheng.net/PixelGaussian

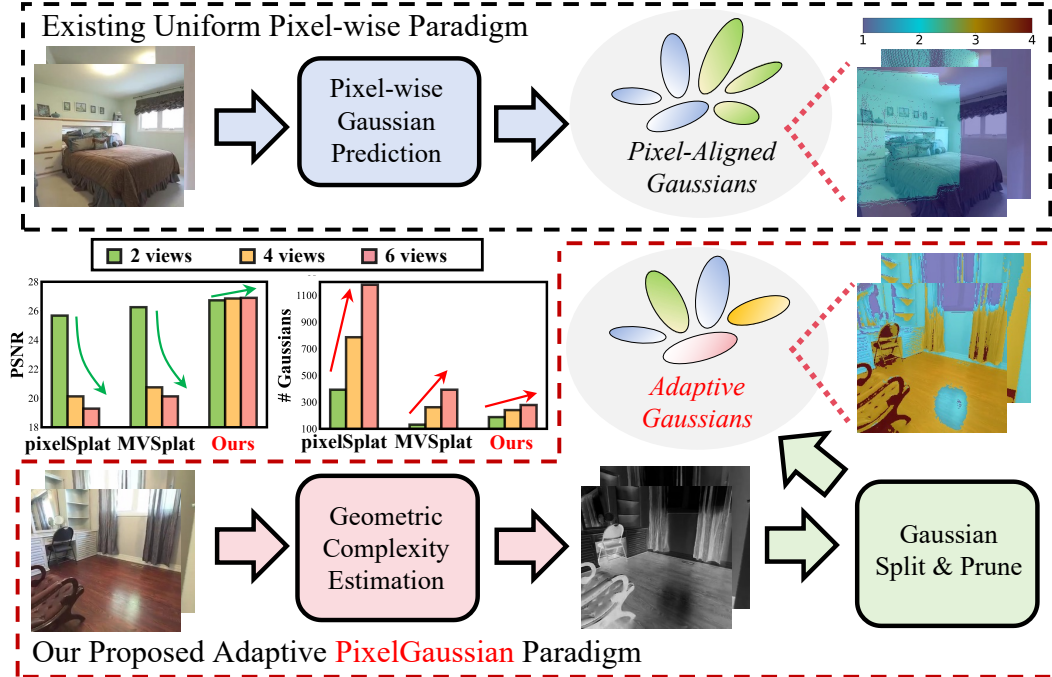Figure 1: Most existing generalizable 3D Gaussian splatting methods (e.g., pixelSplat (Charatan et al., 2023), MVSplat (Chen et al., 2024)) assign a fixed number of Gaussians to each pixel, leading to inefficiency in capturing local geometry and overlap across views. Differently, our PixelGaussian dynamically adjusts the Gaussian distributions based on geometric complexity in a feed-forward framework. With comparable efficiency, PixelGaussian (trained using 2 views) successfully generalizes to various numbers of input views with adaptive Gaussian densities.

ABSTRACT

We propose **PixelGaussian**, an efficient feed-forward framework for learning generalizable 3D Gaussian reconstruction from arbitrary views. Most existing methods rely on uniform pixel-wise Gaussian representations, which learn a fixed number of 3D Gaussians for each view and cannot generalize well to more input views. Differently, our PixelGaussian dynamically adapts both the Gaussian distribution and quantity based on geometric complexity, leading to more efficient representations and significant improvements in reconstruction quality. Specifically, we introduce a Cascade Gaussian Adapter to adjust Gaussian distribution according to local geometry complexity identified by a keypoint scorer. CGA

---

[*]Work done while visiting UC Berkeley.

[†]Corresponding author.

leverages deformable attention in context-aware hypernetworks to guide Gaussian pruning and splitting, ensuring accurate representation in complex regions while reducing redundancy. Furthermore, we design a transformer-based Iterative Gaussian Refiner module that refines Gaussian representations through direct image-Gaussian interactions. Our PixelGaussian can effectively reduce Gaussian redundancy as input views increase. We conduct extensive experiments on the large-scale ACID and RealEstate10K datasets, where our method achieves state-of-the-art performance with good generalization to various numbers of views. Code: https://github.com/Barrybarry-Smith/PixelGaussian.

1 INTRODUCTION

Novel view synthesis (NVS) seeks to reconstruct a 3D scene from a series of input views and generate high-quality images from previously unseen viewpoints. High-quality and real-time reconstruction and view synthesis are crucial for autonomous driving (Tonderski et al., 2023; Khan et al., 2024; Tian et al., 2024; Huang et al., 2024a), robotics perception (Wilder-Smith et al., 2024; Jiang et al., 2023a) and virtual or augmented reality (Yang et al., 2024; Zheng et al., 2024).

NeRF-based methods (Mildenhall et al., 2020; Hu et al., 2022; Liu et al., 2020; Neff et al., 2021) have achieved remarkable success by encoding 3D scenes into implicit radiance fields, yet sampling volumes for NeRF rendering is costly in both time and memory. Recently, Kerbl et al. (2023) proposed to represent 3D scenes explicitly using a set of 3D Gaussians, enabling much more efficient and high-quality rendering via a differentiable rasterizer. Still, the original 3D Gaussian Splatting requires separate optimization on each single scene, which significantly reduces inference efficiency. To tackle this problem, recent researches have aimed at generating 3D Gaussians directly from a feed-forward network without any per-scene optimization (Charatan et al., 2023; Chen et al., 2024; Liu et al., 2024; Szymanowicz et al., 2024; Zheng et al., 2024). Typically, these approaches adhere to a paradigm where a fixed number of Gaussians is predicted for each pixel in the input views. The Gaussians derived from different views are then directly merged to construct the final 3D scene representation. However, such a paradigm limits the model performance as the Gaussian splats are uniformly distributed across images, making it difficult to capture local geometric details effectively. Additionally, as the number of input views increases, directly merging Gaussians can degrade reconstruction performance due to severe Gaussian overlap and redundancy across views.

To address this, we propose **PixelGaussian**, which enables dynamic adaption on both 3D Gaussian distribution and quantity. To be specific, we first uniformly initialize Gaussian positions following Chen et al. (2024) to accurately localize the Gaussian centers. To identify geometry complexity across images, we then compute a relevance score map for each input view from image features in an end-to-end manner. Under the guidance of score maps, we construct a Cascade Gaussian Adapter (CGA), which leverages deformable attention (Xia et al., 2022) to control the pruning and splitting operations. After CGA, more Gaussians are allocated to regions with complex geometry for precise reconstruction, while unnecessary and duplicate Gaussians across views are pruned to reduce redundancy and improve efficiency. Since these Gaussian representations still fall short in fully capturing the image details, we further introduce a transformer-based Iterative Gaussian Refiner (IGR) to refine 3D Gaussians through direct image-Gaussian interactions. Finally, we employ rasterization-based rendering using the refined Gaussians to generate novel views at target viewpoints.

We conduct extensive experiments on ACID (Liu et al.) and RealEstate10K (Zhou et al., 2018) benchmarks for large-scale 3D scene reconstruction and novel view synthesis. PixelGaussian outperforms existing methods on different input views with a comparable inference speed. Notably, existing generalizable 3D Gaussian splatting methods (pixelSplat (Charatan et al., 2023) and MVS-plat (Chen et al., 2024)) fail to achieve good results when transferring to more input views while our method demonstrates consistent performance. This is because existing pixel-wise methods generate uniform pixel-aligned Gaussian predictions, and our model mitigates Gaussian overlap and redundancy across views by dynamically adjusting their distribution based on local geometry complexity. Visualizations and ablations further demonstrate that both CGA and IGR blocks are crucial in adapting Gaussian distribution, enabling the proposed PixelGaussian to capture geometry details and achieve better reconstruction accuracy.

2 RELATED WORK

Multi-View Stereo. Multi-View Stereo (MVS) aims to reconstruct a 3D representation from multi-view images of a given scene or object. Since accurate depth estimation is essential for reliable 3D reconstruction from 2D inputs, most MVS methods (Gu et al., 2020; Ding et al., 2021; Yao et al., 2018) require ground truth depth for supervision in training process. Additionally, point-based MVS approaches generally separate the processes of depth estimation and point cloud fusion processes. Recently, inspired by efficient Gaussian representations proposed by Kerbl et al. (2023), Chen et al. (2024) introduces to directly predict depth for pixel-wise Gaussians from a cost volume structure without requiring depth supervision, significantly improving model scalability and flexibility. Therefore, following a similar approach, we construct a lightweight cost volume to facilitate depth estimation, which serves as an efficient initialization for 3D Gaussians in our PixelGaussian.

Per-scene 3D Reconstruction. Neural Radiance Fields (NeRF) have revolutionized the field of 3D reconstruction by representing scenes as implicit neural fields (Mildenhall et al., 2020). Subsequent researches have focused on overcoming the limitations of the original NeRF to improve its performance and broaden its applicability. Some researches aim to improve the efficiency for novel view synthesis (Hu et al., 2022; Fridovich-Keil et al., 2022; Yu et al., 2021a; Liu et al., 2020; Neff et al., 2021). Moreover, several studies concentrate on capturing intricate geometry and temporal information to achieve accurate and dynamic reconstruction (Li et al., 2021; Du et al., 2021; Pumarola et al., 2020; Tian et al., 2023; Wang et al., 2022). Compared to implicit NeRF-based methods, 3D Gaussian Splatting (3DGS) (Kerbl et al., 2023) represents a 3D scenario as a set of explicit 3D Gaussians, enabling a rasterization-based splatting rendering process that is significantly more efficient in both time and memory. Given that 3DGS still requires millions of 3D Gaussians to represent a single scene, numerous studies have focused on achieving real-time rendering and minimizing memory usage (Fan et al., 2023; Katsumata et al., 2024; Lu et al., 2024). Additionally, some researches focus on enhancing the reconstruction quality of 3DGS by employing multi-scale rendering (Yan et al., 2024), advanced shading models (Jiang et al., 2023b) or incorporating physically based properties for realistic relighting (Gao et al., 2023). However, these methods still require per-scene optimization and rely on dense input views, which can be computationally expensive and limit their scalability for large-scale or dynamic scenes.

Generalizable 3D Reconstruction. PixelNeRF (Yu et al., 2021b) pioneers the approach of predicting pixel-wise features directly from input views to reconstruct neural radiance fields. Following methods incorporate volume or transformer architectures to improve the performance of feed-forward NeRF models (Chen et al., 2021a; Xu et al., 2024; Miyato et al., 2024; Sajjadi et al., 2022; Du et al., 2023). However, these feed-forward NeRF approaches typically demand substantial memory and computational resources due to the expensive per-pixel volume sampling process (Wang et al., 2021a; Johari et al., 2022; Barron et al., 2021; Garbin et al., 2021; Reiser et al., 2021; Müller et al., 2022). With the advent of 3DGS, PixelSplat (Charatan et al., 2023) initiates a shift towards feed-forward Gaussian-based reconstruction. It takes sparse input views to directly predict pixel-wise 3D Gaussians by leveraging epipolar geometry to learn cross-view features. MVSplat (Chen et al., 2024) constructs a cost volume structure for depth estimation, which significantly boosts both model efficiency and reconstruction quality. Additionally, MVSGaussian (Liu et al., 2024) further improves model performance by introducing an efficient hybrid Gaussian rendering process. Moreover, SplatterImage (Szymanowicz et al., 2024) and GPS-Gaussian (Zheng et al., 2024) predict pixel-wise 3D Gaussians for object-centric or human reconstruction.

However, these feed-forward methods are constrained by the pixel-wise Gaussian prediction paradigm, which limits the model's performance as the Gaussian splats are uniformly distributed across images. Such a paradigm inadequately captures intricate geometries, while also causing Gaussian overlap and redundancy across views, ultimately resulting in severe rendering artifacts. In comparison, PixelGaussian consists of a Cascade Gaussian Adapter (CGA), allowing for dynamic adaption on both Gaussian distribution and quantity. Visualizations demonstrate that CGA is capable of allocating more Gaussians in areas rich in geometric details, while reducing duplicate Gaussians in similar regions across input views. Furthermore, we introduce an Iterative Gaussian Refiner (IGR), enabling direct interaction between 3D Gaussians and local image features via deformable attention. Experimental results show that IGR effectively leverages image features to guide Gaussians in capturing the full information contained within the images, significantly enhancing the model's ability to capture local intricate geometry.
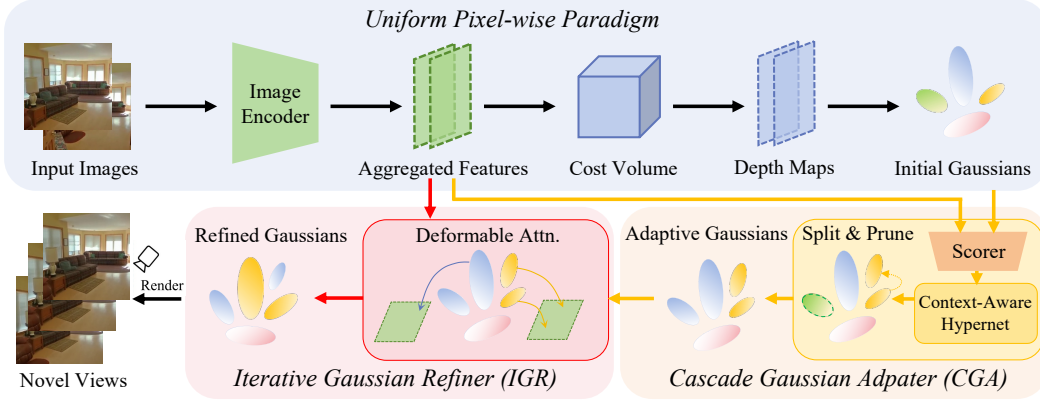
Figure 2: **Overview of PixelGaussian.** Given multi-view input images, we initialize 3D Gaussians using a lightweight image encoder and cost volume. Cascade Gaussian Adapter (CGA) then dynamically adapts both the distribution and quantity of Gaussians. By leveraging local image features, Iterative Gaussian Refiner (IGR) further refines Gaussian representations via deformable attention. Finally, novel views are rendered from the refined 3D Gaussians using rasterization-based rendering.

3 PROPOSED APPROACH

In this section, we present our method to learn generalizable Gaussian representations from arbitrary views. Given an arbitrary set of input images $\mathcal{I} = \{I_i\}_{i=1}^N \in \mathbb{R}^{N \times H \times W \times 3}$ and corresponding camera poses $\mathcal{C} = \{C_i\}_{i=1}^N$, our PixelGaussian aims to learn a mapping $\mathcal{M}$ from images to 3D Gaussians for scene reconstruction:

$$\mathcal{M} : \{(I_i, C_i)\}_{i=1}^N \mapsto \{(\mu_j, s_j, r_j, \alpha_j, sh_j)\}_{j=1}^{N_K}, \tag{1}$$

where N_K is the total number of 3D Gaussians, which adaptively varies depending on the scene context. Each Gaussian is parameterized by its position μ_j, scaling s_j, rotation r_j, opacity α_j and spherical harmonics sh_j.

As illustrated in Figure 2, we first use a lightweight cost volume for depth estimation and Gaussian position initialization. We then introduce Cascade Gaussian Adapter (CGA), which dynamically adapts both Gaussian distribution and quantity based on local geometric complexity. Finally, we explain how Iterative Gaussian Refiner (IGR) enables direct image-Gaussian interactions, further refining Gaussian distribution and representations for enhanced reconstruction.

3.1 GAUSSIAN INITIALIZATION

Position Initialization. Following the instructions of MVSplat (Chen et al., 2024), we first extract image features via a 2D backbone consisting of CNN and Swin Transformer (Liu et al., 2021). Specifically, CNN encodes multi-view images to corresponding feature maps, while Swin Transformer performs both self-attention and cross-view attention to better leverage information cross views. Then, we obtain the aggregated multi-view features $\mathcal{F} = \{F_i\}_{i=1}^N$.

To initialize Gaussian positions precisely, we construct a lightweight cost volume (Yao et al., 2018) for depth estimation, denoted as Φ_{depth}. We then predict Gaussian centers as follows:

$$\mu = P^{-1}(\Phi_{depth}(\mathcal{F}), \mathcal{C}) \tag{2}$$

where $P^{-1}(\cdot)$ stands for unprojection operation.

Parameter Initialization. For each Gaussian center μ_j, we randomly set corresponding scaling $s_j \in \mathbb{R}^3$, rotation $r_j \in \mathbb{R}^4$, opacity $\alpha_j \in \mathbb{R}^1$, spherical harmonics $sh_j \in \mathbb{R}^C$ within a proper range. we then get the initial Gaussians set $\mathcal{G} = \{(\mu_j, s_j, r_j, \alpha_j, sh_j)\}_{j=1}^{HW} \in \mathbb{R}^{HW \times (11+C)}$.

3.2 CGA: CASCADE GAUSSIAN ADAPTER

After obtaining the initial Gaussian set $\mathcal{G}$, we introduce Cascade Gaussian Adapter (CGA) driven by a multi-view keypoint scorer Ψ, as shown in Figure 3(a). CGA contains a set of context-aware
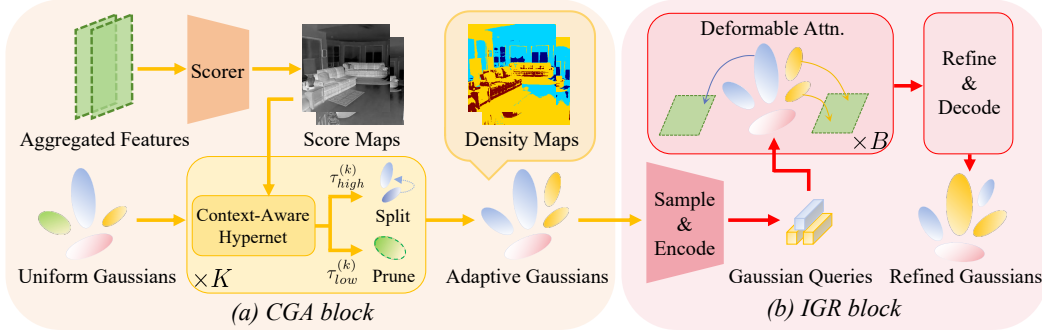
Figure 3: **Illustration of the proposed CGA and IGR Blocks.** (a) CGA comprises a keypoint scorer followed by a series of hypernetworks that produce context-aware thresholds to guide the splitting and pruning of Gaussians. (b) IGR further facilitates direct image-Gaussian interactions, enabling Gaussian representations to capture and extract local geometric features more effectively.

hypernetworks $\mathcal{H}$ which dynamically control and guide the following Gaussian pruning and splitting operations. This approach ensures that regions with complex geometry details are represented by a greater number of Gaussians, while areas with poor geometry can be represented with fewer Gaussians. In parallel, CGA effectively removes redundant Gaussians to prevent Gaussian overlap across views. Compared to previous pixel-wise methods, which rigidly allocate a fixed number of Gaussians per pixel, our design dynamically adapts both distribution and quantity of Gaussians based on geometric complexity. This flexibility allows for a more accurate capture of local geometry and mitigates the problem of Gaussian overlap, thereby improving the overall quality of reconstruction.

Given the aggregated features $\mathcal{F}$ derived in Section 3.1, Ψ computes relevance score maps $\mathcal{R} = \{R_i\}_{i=1}^N \in \mathbb{R}^{N \times H \times W}$, where each score map R_i is obtained by a learnable weighted average of contributions from different views:

$$\mathcal{R} = \Psi(\mathcal{F}) = softmax\left(MLP\left(\sum_{i=1}^N \alpha_i \cdot F_i\right)\right), \quad \alpha_i = \frac{\exp(\beta_i)}{\sum_{j=1}^N \exp(\beta_j)}, \tag{3}$$

where $A = [\alpha_1, \alpha_2, \ldots, \alpha_N]^T \in \mathbb{R}^N$ represents the contribution factor of each view, and is determined by learnable parameters $\beta_i (i = 1, 2, ..., N)$.

We first introduce a set of hypernetworks $\mathcal{H} = \{H_k\}_{k=1}^K$ to generate *context-aware* thresholds. CGA is composed of K stages, where each stage H_k takes score maps $\mathcal{R}$ along with Gaussian set $\mathcal{G}_k = \{(\mu_j^{(k)}, s_j^{(k)}, r_j^{(k)}, \alpha_j^{(k)}, sh_j^{(k)})\}_{j=1}^{N_k} \in \mathbb{R}^{N_k \times (11+C)}$ as input, and outputs thresholds $\tau_{high}^{(k)}, \tau_{low}^{(k)} \in \mathbb{R}$ for splitting and pruning. As illustrated in equation 4, we first sample and embed Gaussian set $\mathcal{G}_k$ into Gaussian score queries $\mathcal{Q}_r^{(k)}$. Then we project sampled reference points $\mu^{(k)}$ onto score maps $\mathcal{R}$ with corresponding camera parameters $\mathcal{C}$. Finally, we update queries $\mathcal{Q}_r^{(k)}$ with weighted scores from $\mathcal{S}$ and get both thresholds through a simple MLP. Initially, we set $\mathcal{G}_1 = \mathcal{G}$.

$$\tau_{high}^{(k)}, \tau_{low}^{(k)} = \mathcal{H}_k(\mathcal{G}_k, \mathcal{R}, \mathcal{C}) = MLP(\sum_{i=1}^N \alpha_i \cdot DA(\mathcal{Q}_r^{(k)}, R_i, P(\mu^{(k)}, C_i))), \tag{4}$$

where $DA(\cdot), P(\cdot)$ denote the deformable attention function and projection operation, respectively.

Then, we obtain Gaussian-wise scores by projecting Gaussian centers onto score maps $\mathcal{R}$. To elaborate, let $S_k = \{s_{ij}^{(k)}\} \in \mathbb{R}^{N \times N_k}$ be the score matrix for Gaussian set $\mathcal{G}_k$, where each score $s_{ij}^{(k)}$ is the value at the projection point of the $j - th$ Gaussian center in R_i, or 0 if it does not project onto any region in R_i. The final Gaussian-wise scores S_k^{avg} are then computed by averaging scores across different views:

$$S_k^{avg} = S_k^T \cdot A, \tag{5}$$

Once Gaussian-wise scores are obtained, regions with higher scores, indicating more complex geometry details, undergo splitting operation to allocate more Gaussians for finer representations. For regions with lower scores, we apply an opacity-based pruning operation, gradually reducing Gaussian opacity and scaling to minimize their impact and reduce redundancy.

Splitting. For Gaussian $g_j^{(k)} \in \mathcal{G}_k$ with score higher than $\tau_{\text{high}}^{(k)}$, we generate M separate new Gaussians for more detailed representations:

$$G_j^{(k)} = SplitNet(g_j^{(k)}) \in \mathbb{R}^{M \times (11+C)}, \tag{6}$$

where $SplitNet(\cdot)$ is a simple MLP-based network that ensures all parameters within proper range. The newly generated Gaussians are then directly concatenated with the existing Gaussian set $\mathcal{G}_k$.

Pruning. For Gaussian $g_j^{(k)} \in \mathcal{G}_k$ with score lower than $\tau_{\text{low}}^{(k)}$, we apply an opacity-based pruning operation rather than directly removing it. Specifically, we set a predefined opacity threshold τ_α. If the Gaussian opacity is greater than τ_α, we gradually reduce its opacity and scaling:

$$\alpha_j^{(k)} \to \gamma_\alpha \cdot \alpha_j^{(k)}, \quad s_j^{(k)} \to \gamma_s \cdot s_j^{(k)}, \tag{7}$$

where $\gamma_\alpha < 1$ and $\gamma_s < 1$ are reduction factors. Otherwise, the current Gaussian is removed entirely from Gaussian set $\mathcal{G}_k$.

After K-stage adaptation in the Cascade Gaussian Adapter, the initial uniform 3D Gaussian representations are transformed into adaptive forms. Gaussians are redistributed according to geometric complexity, resulting in a more efficient and context-aware representation.

3.3 IGR: Iterative Gaussian Refiner

Though CGA allows for a more optimal Gaussian distribution, the Gaussian representations still fall short in capturing the full information contained in the images. Inspired by the efficiency demonstrated by GaussianFormer (Huang et al., 2024b) in occupancy prediction, we design a transformer-based Iterative Gaussian Refiner (IGA) to further extract local geometric information from input views, as shown in Figure 3(b). In this process, we leverage deformable attention to enable direct image-Gaussian interactions, enhancing the ability for 3D Gaussians to more accurately capture intricate geometry details in reconstruction and view synthesis.

IGR is composed of B attention and refinement blocks. In Section 3.2, CGA adapts the original Gaussian set $\mathcal{G}$ to $\mathcal{G} = \mathcal{G}_K$. To continue, we first sample and embed $\mathcal{G}$ into Gaussian queries $\mathcal{Q}$. In each block, deformable attention is first applied between Gaussian queries $\mathcal{Q}$ and multi-view features $\mathcal{F}$ to update Gaussian representations. This is followed by a refinement stage where a residual module further fine-tunes the queries. The overall process of IGR can be formulated as:

$$\mathcal{Q}_b = \Phi_{ref}\left(\sum_{i=1}^{N} \alpha_i \cdot DA(\mathcal{Q}_{b-1}, F_i, P(\mu^{(b)}, C_i))\right) \quad b = 1, 2, \ldots, B, \tag{8}$$

where $DA(\cdot), \Phi_{ref}(\cdot), P(\cdot)$ denote the deformable attention function, refinement layer and projection operation, F_i, C_i, α_i represents the image feature, camera parameters and contribution factor of input view I_i, respectively. $\mathcal{Q}_b(b = 1, 2, ..., B)$ stands for output queries from the $b-th$ IGR block, and $\mu^{(b)}$ is the Gaussian center of current stage. Initially, we set $\mathcal{Q}_0 = \mathcal{Q}$.

Finally, the refined Gaussian queries are decoded into Gaussian parameters $\mathcal{G}_f$ through a simple MLP to ensure all parameters within proper range, and then can be used for rasterization-based rendering at novel viewpoints.

$$\mathcal{G}_f = \{(\mu_j^f, s_j^f, r_j^f, \alpha_j^f, sh_j^f)\}_{j=1}^{N_K} = MLP(\mathcal{Q}_B). \tag{9}$$

Our full model takes ground-truth target RGB images at novel viewpoints as supervision, allowing for efficient end-to-end training. The training loss is calculated as a linear combination of MSE and LPIPS (Zhang et al., 2018) losses, with loss weights of 1 and 0.05, respectively.

Table 1: **Results of Novel View Synthesis on the RealEstate10K and ACID benchmarks.** We report the average PSNR and LPIPS (Zhang et al., 2018) on the test set, where all models are trained with 2 reference views and <mark>inferred with 2, 3, and 4 reference views.</mark>

Datasets	Methods	2→2 Views		2→3 Views		2→4 Views	
		PSNR↑	LPIPS↓	PSNR↑	LPIPS↓	PSNR↑	LPIPS↓
RealEstate10K	pixelNeRF	20.25	0.556	21.15	0.525	21.68	0.518
	MuRF	25.95	0.146	26.23	0.137	26.40	0.134
	pixelSplat	25.67	0.145	22.35	0.242	20.12	0.283
	MVSplat	26.25	0.130	22.94	0.236	20.74	0.268
	PixelGaussian	**26.72**	**0.126**	**26.79**	**0.123**	**26.85**	**0.122**
ACID	pixelNeRF	20.66	0.530	21.33	0.518	21.40	0.506
	MuRF	27.94	0.163	28.22	0.154	28.35	0.149
	pixelSplat	28.06	0.152	23.73	0.276	20.15	0.294
	MVSplat	28.26	0.144	23.85	0.268	20.32	0.275
	PixelGaussian	**28.63**	**0.140**	**28.72**	**0.137**	**28.78**	**0.137**

Compared to the uniform pixel-wise paradigm, our PixelGaussian approach dynamically adapts both the Gaussian distribution and quantity within the Cascade Gaussian Adapter. Additionally, the Iterative Gaussian Refiner refines Gaussian representations to capture intricate geometric details in the input views. This design achieves more efficient Gaussian distributions while mitigating overlap and redundancy common in pixel-wise methods.

4 EXPERIMENTS

4.1 EXPERIMENTAL SETTINGS

Datasets. To assess the performance of our model, we conduct experiments on two extensive datasets: ACID (Liu et al.) and RealEstate10K (Zhou et al., 2018). The ACID dataset consists of video frames capturing natural landscape scenes, comprising 11,075 scenes in the training set and 1,972 scenes in the test set. RealEstate10K provides video frames from real estate environments, with 67,477 scenes allocated for training and 7,289 scenes reserved for testing. The model is trained with two reference views, and four novel views are selected for evaluation. During testing, however, we perform multiple experiments where 2, 3, and 4 views are selected for reference, while four novel views selected for evaluation in each scenario.

Implementation Details. We set the resolutions of input images as 256x256. In Cascade Gaussian Adapter (CGA), we apply $K = 3$ stages of cascade Gaussian adaption. As for the splitting operation, the SplitNet generates $M = 1$ separate new Gaussians, whereas the pruning process uses reduction factors $\gamma_\alpha = \gamma_s = 0.5$ and opacity threshold $\tau_\alpha = 0.3$. We use $B = 3$ blocks in Iterative Gaussian Refiner (IGR) to extract local geometry from input views. We implement our PixelGaussian with Pytorch and train the model on 8 NVIDIA A6000 GPUs for 300,000 iterations with Adam optimizer. More training details are provided in Section A.2.

4.2 MAIN RESULTS

Novel View Synthesis. As shown in Table 1 and Figure 4, our proposed PixelGaussian consistently outperforms previous NeRF-based methods and pixel-wise Gaussian feed-forward networks across all settings with 2, 3, and 4 reference views. Notably, as the number of input views increases, the reconstruction performance of both pixelSplat (Charatan et al., 2023) and MVSplat (Chen et al., 2024) degrades significantly, while PixelGaussian shows a slight improvement. This is because previous methods directly merge multiple views by back-projecting pixel-wise Gaussians to 3D space based on depth maps. Without the capability to adapt the quantity and distribution of Gaussians dynamically, pixel-wise methods often produce duplicated Gaussians with significant overlap, and their spatial positioning is suboptimal. In contrast, PixelGaussian is able to optimize both the distribution and quantity of Gaussians via CGA, while IGR blocks facilitate direct interaction between Gaussian queries and local image features, resulting in more accurate reconstructions.

Figure 4: **Visualization results on ACID and RealEstate10K benchmarks.** Pixel-wise methods suffer from Gaussian overlap due to suboptimal Gaussian distributions, whereas PixelGaussian enables dynamic Gaussian adaption and improved local geometry refinement.

Table 2: **Comparison of PSNR and Gaussian Quantity on RealEstate10K Dataset.** We present the average PSNR and the number of Gaussians (K) for inference using 2, 4, and 6 input views.

Methods	2→2 Views		2→4 Views		2→6 Views	
	PSNR↑	# Gaussians	PSNR↑	# Gaussians	PSNR↑	# Gaussians
pixelSplat	25.67	393 K	20.12	786 K	19.36	1179 K
MVSplat	26.25	**131 K**	20.74	262 K	20.24	393 K
PixelGaussian	**26.72**	188 K	**26.85**	**240 K**	**26.89**	**278 K**

Multi-View Comparison. We further compare model performance and Gaussian quantities of different methods across various input views in Table 2. Though our method requires more Gaussians than MVSplat (Chen et al., 2024) with 2 input views due to more frequent splitting than pruning, it achieves better reconstruction with fewer Gaussians as the number of views increases. In regions with richer geometric details, CGA blocks first split more Gaussians for finer representations, followed by IGR to further refine these Gaussians using deformable attention on local image features to better capture and reconstruct geometric details. Meanwhile, CGA prunes duplicate and overlapping Gaussians across views to control the growth of overall Gaussian quantity as the number of input views increases.

Efficiency Analysis. We explore the efficiency of PixelGaussian compared with dominant pixel-wise methods on a single NVIDIA A6000 GPU. All models are inferred with 4 input views on the RealEstate10K (Zhou et al., 2018) dataset. We report the average inference latency, memory cost, number of Gaussians and rendering FPS in Table 3. Undeniably, PixelGaussian requires higher latency and memory usage than MVSplat (Chen et al., 2024) due to the extra cost of CGA and IGR blocks. However, this trade-off allows PixelGaussian to achieve higher rendering FPS by utilizing fewer Gaussians and far more better reconstruction quality as the number of input view increases.

4.3 EXPEIMENTAL ANALYSIS

In this section, we further investigate and conduct experiments to demonstrate the effectiveness of our PixelGaussian. We first visualize the score maps $\mathcal{S}$ and Gaussian density maps. Then, we present the cascade adaption process of CGA. Finally, we conduct ablation studies on our model. These

Table 3: **Efficiency analysis.** Inference on RealEstate10K (Zhou et al., 2018) dataset using 4 input views, reporting average latency, memory cost, Gaussian quantity, and rendering FPS.

Methods	Latency	Memory	# Gaussians	Rendering FPS
pixelSplat	298 ms	11.78 G	786 K	64
MVSplat	**126 ms**	**3.17 G**	262 K	133
PixelGaussian	235 ms	4.39 G	**240 K**	**140**

			Gaussian density (Gaussian / pixel)

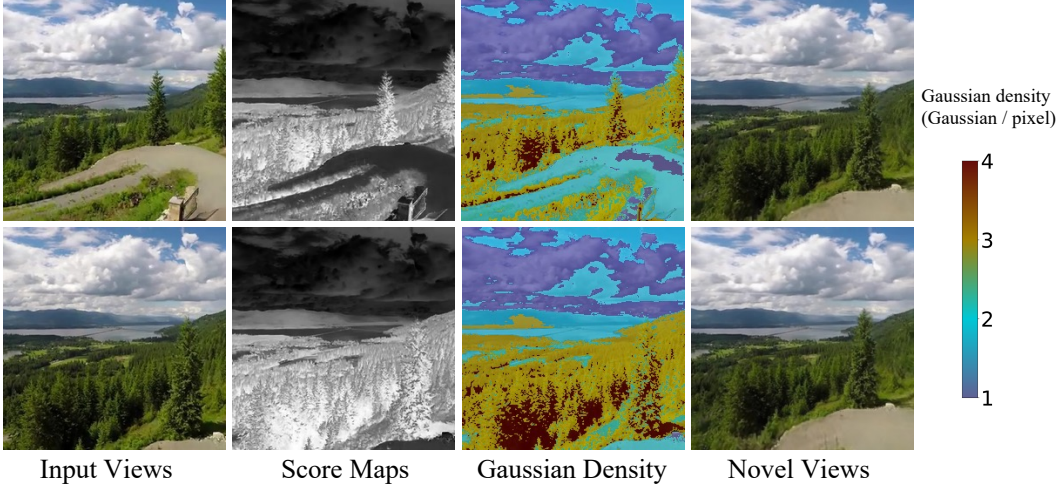Input Views   Score Maps   Gaussian Density   Novel Views

Figure 5: **Visualization of score maps and Gaussian distributions on RealEstate10K dataset.** Cascade Gaussian Adapter dynamically adjusts Gaussian distribution and quantity based on score maps. More Gaussians are allocated to detail-rich regions for more precise representations, while pruning minimizes Gaussian redundancy and overlap across views.

experiments show that CGA dynamically adapts both the distribution and quantity of Gaussians according to geometric complexity, while IGR further extract local features via direct image-Gaussian interactions, offering significant improvements over traditional pixel-wise methods.

Score Maps and Density Maps. As shown in 3, relevance score maps $\mathcal{S}$ are derived from multi-view image features through the keypoint scorer Ψ. To further understand the significance of $\mathcal{S}$ and its impact on the subsequent Gaussian splitting and pruning operations, we visualize the relevance score maps on the RealEstate10K (Zhou et al., 2018) dataset. Furthermore, we project the centers of the adaptive Gaussian after CGA $(i.e. \{\mu_j^f\}_{j=1}^{N_K})$, onto each input view as Gaussian density maps. Figure 5 illustrates that in this end-to-end learning framework, keypoint scorer Ψ is able to learn such score maps where local regions with richer and more complex geometric details tend to receive higher score, which guides the following SplitNet to allocate more Gaussians for more precise representations. In contrast, regions with fewer geometric details receive lower scores, leading to pruning to reduce representation complexity while preserving overall representation efficiency.

Cascade Gaussian Adaption. To present the cascade Gaussian adaption process in CGA blocks more explicitly, we visualize Gaussian density maps during model inference on the RealEstate10K (Zhou et al., 2018) dataset with 2 input views. As illustrated in Figure 6, the original Gaussian set $\mathcal{G}$ is initialized on a pixel-wise basis. Following this, score maps $\mathcal{S}$ guide hypernetworks $\mathcal{H}$ to generate context-aware thresholds, which in turn direct the subsequent Gaussian splitting and pruning operations. More Gaussians are allocated in regions with richer geometric details, while duplicate Gaussians across views tend to be pruned, leading to a more efficient and optimal Gaussian distribution for scene representation.

Ablation Study. To further investigate the architecture of PixelGaussian, we conduct ablation studies by inferring our model on RealEstate10K (Zhou et al., 2018) test dataset with 4 input views. We first introduce a vanilla model, where the initial Gaussian set $\mathcal{G}$ is directly used to render novel views. Then, we adopt rigid CGA blocks without context-aware Hypernetworks $\mathcal{H}$, which means Gaussian set $\mathcal{G}$ goes through splitting and pruning based on fixed thresholds $(\tau_{high}^{(k)} = 0.8, \tau_{low}^{(k)} = 0.2, k = 1, 2, ..., K)$. We further add HyperNetworks $\mathcal{H}$ to generate context-
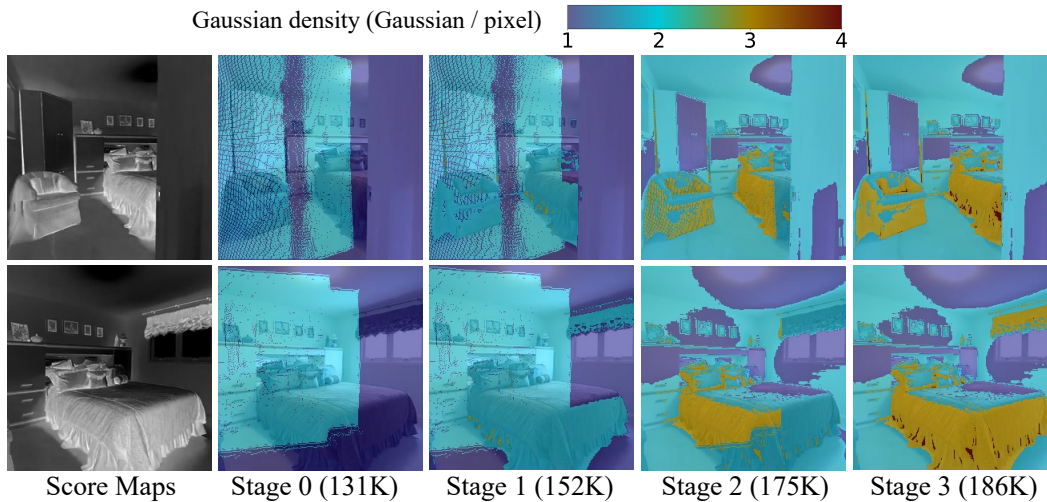
Figure 6: **Visualization of Gaussian adaption process in Cascade Gaussian Adapter.** During inference on RealEstate10K (Zhou et al., 2018) dataset, CGA progressively concentrates more Gaussians on geometrically complex regions, while pruning duplicate Gaussians across views to control the growth of overall Gaussian quantity.

Table 4: **Ablations on the components of PixelGaussian.** We report the average PSNR, LPIPS (Zhang et al., 2018), and the number of Gaussians (K) of model inference.

Methods	PSNR↑	LPIPS↓	#Gaussians
Vanilla	20.34	0.272	262 K
+ Rigid Cascade Gaussian Adapter	22.46	0.220	225 K
+ HyperNetworks $\mathcal{H}$	25.80	0.140	**240 K**
+ Iterative Gaussian Refiner	**26.85**	**0.122**	**240 K**

aware thresholds. Finally, we adopt IGR blocks to refine the Gaussian representations via image-Gaussian interactions. As shown in Table 4, HyperNetworks $\mathcal{H}$ utilizes score maps $\mathcal{S}$ to generate context-aware thresholds, enabling a more dynamic and efficient Gaussian distribution for scene representation compared to rigid splitting and pruning. Furthermore, IGR blocks refine the Gaussian set iteratively via deformable attention between Gaussians and image features, enhancing their ability to describe and reconstruct intricate local geometric details.

5 CONCLUSION AND DISCUSSIONS

In this paper, we have presented PixelGaussian to learn generalizable 3D Gaussian reconstruction from arbitrary input views. The core innovation of our approach is *context-aware* Cascade Gaussian Adapter (CGA), which dynamically splits Gaussians in regions with complex geometric details and prunes redundant ones. Further, we incorporate deformable attention within Iterative Gaussian Refiner (IGR), facilitating direct image-Gaussian interactions to improve local geometry reconstructions. Compared to previous uniform pixel-wise methods, PixelGaussian is able to dynamically adapt both Gaussian distribution and quantity guided by the complexity of local geometry details, allocating more to detailed regions and reducing redundancy across views, thus leading to better performance in reconstruction and view synthesis.

Discussions and Limitations. Although PixelGaussian can adjust the distribution of 3D Gaussians dynamically, the initial Gaussians are still derived from pixel-wise unprojection. When we initialize the Gaussian centers completely at random, the model fails to converge. Moreover, deformable attention in IGR consumes substantial computational resources when the number of Gaussians is extremely large, highlighting the need for a more efficient approach to represent 3D scenes with fewer Gaussians. Furthermore, PixelGaussian is unable to perceive the unseen parts of 3D scenes beyond the input views, suggesting the potential need to incorporate generative models.

REFERENCES

Jonathan T. Barron, Ben Mildenhall, Matthew Tancik, Peter Hedman, Ricardo Martin-Brualla, and Pratul P. Srinivasan. Mip-nerf: A multiscale representation for anti-aliasing neural radiance fields, 2021.

David Charatan, Sizhe Li, Andrea Tagliasacchi, and Vincent Sitzmann. pixelsplat: 3d gaussian splats from image pairs for scalable generalizable 3d reconstruction. In *arXiv*, 2023.

Anpei Chen, Zexiang Xu, Fuqiang Zhao, Xiaoshuai Zhang, Fanbo Xiang, Jingyi Yu, and Hao Su. Mvsnerf: Fast generalizable radiance field reconstruction from multi-view stereo. *arXiv preprint arXiv:2103.15595*, 2021a.

Chun-Fu (Richard) Chen, Rameswar Panda, and Quanfu Fan. RegionViT: Regional-to-Local Attention for Vision Transformers. In *ArXiv*, 2021b.

Yuedong Chen, Haofei Xu, Chuanxia Zheng, Bohan Zhuang, Marc Pollefeys, Andreas Geiger, Tat-Jen Cham, and Jianfei Cai. Mvsplat: Efficient 3d gaussian splatting from sparse multi-view images. *arXiv preprint arXiv:2403.14627*, 2024.

Zhiyang Chen, Yousong Zhu, Chaoyang Zhao, Guosheng Hu, Wei Zeng, Jinqiao Wang, and Ming Tang. Dpt: Deformable patch-based transformer for visual recognition. In *ACM MM*. ACM, October 2021c.

Christopher B. Choy, Danfei Xu, JunYoung Gwak, Kevin Chen, and Silvio Savarese. 3d-r2n2: A unified approach for single and multi-view 3d object reconstruction, 2016.

Yikang Ding, Wentao Yuan, Qingtian Zhu, Haotian Zhang, Xiangyue Liu, Yuanjiang Wang, and Xiao Liu. Transmvsnet: Global context-aware multi-view stereo network with transformers, 2021.

Xiaoyi Dong, Jianmin Bao, Dongdong Chen, Weiming Zhang, Nenghai Yu, Lu Yuan, Dong Chen, and Baining Guo. Cswin transformer: A general vision transformer backbone with cross-shaped windows, 2022.

Alexey Dosovitskiy, Lucas Beyer, Alexander Kolesnikov, Dirk Weissenborn, Xiaohua Zhai, Thomas Unterthiner, Mostafa Dehghani, Matthias Minderer, Georg Heigold, Sylvain Gelly, Jakob Uszkoreit, and Neil Houlsby. An image is worth 16x16 words: Transformers for image recognition at scale, 2021.

Yilun Du, Yinan Zhang, Hong-Xing Yu, Joshua B. Tenenbaum, and Jiajun Wu. Neural radiance flow for 4d view synthesis and video processing. In *ICCV*, 2021.

Yilun Du, Cameron Smith, Ayush Tewari, and Vincent Sitzmann. Learning to render novel views from wide-baseline stereo pairs. *CVPR*, 2023.

Zhiwen Fan, Kevin Wang, Kairun Wen, Zehao Zhu, Dejia Xu, and Zhangyang Wang. Lightgaussian: Unbounded 3d gaussian compression with 15x reduction and 200+ fps, 2023.

Sara Fridovich-Keil, Alex Yu, Matthew Tancik, Qinhong Chen, Benjamin Recht, and Angjoo Kanazawa. Plenoxels: Radiance fields without neural networks. In *CVPR*, 2022.

Jian Gao, Chun Gu, Youtian Lin, Hao Zhu, Xun Cao, Li Zhang, and Yao Yao. Relightable 3d gaussian: Real-time point cloud relighting with brdf decomposition and ray tracing. *arXiv:2311.16043*, 2023.

Stephan J Garbin, Marek Kowalski, Matthew Johnson, Jamie Shotton, and Julien Valentin. Fastnerf: High-fidelity neural rendering at 200fps. *arXiv preprint arXiv:2103.10380*, 2021.

Xiaodong Gu, Zhiwen Fan, Zuozhuo Dai, Siyu Zhu, Feitong Tan, and Ping Tan. Cascade cost volume for high-resolution multi-view stereo and stereo matching, 2020.

Kaiming He, Xiangyu Zhang, Shaoqing Ren, and Jian Sun. Deep residual learning for image recognition. In *CVPR*, 2016.

Tao Hu, Shu Liu, Yilun Chen, Tiancheng Shen, and Jiaya Jia. Efficientnerf: Efficient neural radiance fields. In *CVPR*, pp. 12902–12911, June 2022.

Nan Huang, Xiaobao Wei, Wenzhao Zheng, Pengju An, Ming Lu, Wei Zhan, Masayoshi Tomizuka, Kurt Keutzer, and Shanghang Zhang. S^3gaussian: Self-supervised street gaussians for autonomous driving. *arXiv preprint arXiv:2405.20323*, 2024a.

Yuanhui Huang, Wenzhao Zheng, Yunpeng Zhang, Jie Zhou, and Jiwen Lu. Gaussianformer: Scene as gaussians for vision-based 3d semantic occupancy prediction. *arXiv preprint arXiv:2405.17429*, 2024b.

Andrew Jaegle, Felix Gimeno, Andrew Brock, Andrew Zisserman, Oriol Vinyals, and Joao Carreira. Perceiver: General perception with iterative attention, 2021.

Mengqi Ji, Juergen Gall, Haitian Zheng, Yebin Liu, and Lu Fang. Surfacenet: An end-to-end 3d neural network for multiview stereopsis. In *ICCV*, pp. 2307–2315, 2017.

Chenxing Jiang, Hanwen Zhang, Peize Liu, Zehuan Yu, Hui Cheng, Boyu Zhou, and Shaojie Shen. H_2-mapping: Real-time dense mapping using hierarchical hybrid representation. *IEEE Robotics and Automation Letters*, 8(10):6787–6794, October 2023a. ISSN 2377-3774.

Yingwenqi Jiang, Jiadong Tu, Yuan Liu, Xifeng Gao, Xiaoxiao Long, Wenping Wang, and Yuexin Ma. Gaussianshader: 3d gaussian splatting with shading functions for reflective surfaces, 2023b.

M. Johari, Y. Lepoittevin, and F. Fleuret. Geonerf: Generalizing nerf with geometry priors. In *CVPR*, 2022.

Kai Katsumata, Duc Minh Vo, and Hideki Nakayama. A compact dynamic 3d gaussian representation for real-time dynamic view synthesis, 2024.

Bernhard Kerbl, Georgios Kopanas, Thomas Leimkühler, and George Drettakis. 3d gaussian splatting for real-time radiance field rendering. *ACM Transactions on Graphics*, 42(4), July 2023.

Mustafa Khan, Hamidreza Fazlali, Dhruv Sharma, Tongtong Cao, Dongfeng Bai, Yuan Ren, and Bingbing Liu. Autosplat: Constrained gaussian splatting for autonomous driving scene reconstruction, 2024.

Zhengqi Li, Simon Niklaus, Noah Snavely, and Oliver Wang. Neural scene flow fields for space-time view synthesis of dynamic scenes. In *CVPR*, 2021.

Andrew Liu, Richard Tucker, Varun Jampani, Ameesh Makadia, Noah Snavely, and Angjoo Kanazawa. Infinite nature: Perpetual view generation of natural scenes from a single image. In *ICCV*.

Lingjie Liu, Jiatao Gu, Kyaw Zaw Lin, Tat-Seng Chua, and Christian Theobalt. Neural sparse voxel fields. *NeurIPS*, 2020.

Tianqi Liu, Guangcong Wang, Shoukang Hu, Liao Shen, Xinyi Ye, Yuhang Zang, Zhiguo Cao, Wei Li, and Ziwei Liu. Mvsgaussian: Fast generalizable gaussian splatting reconstruction from multi-view stereo. *arXiv preprint arXiv:2405.12218*, 2024.

Ze Liu, Yutong Lin, Yue Cao, Han Hu, Yixuan Wei, Zheng Zhang, Stephen Lin, and Baining Guo. Swin transformer: Hierarchical vision transformer using shifted windows. In *ICCV*, 2021.

Tao Lu, Mulin Yu, Linning Xu, Yuanbo Xiangli, Limin Wang, Dahua Lin, and Bo Dai. Scaffold-gs: Structured 3d gaussians for view-adaptive rendering. In *CVPR*, pp. 20654–20664, 2024.

Ben Mildenhall, Pratul P. Srinivasan, Matthew Tancik, Jonathan T. Barron, Ravi Ramamoorthi, and Ren Ng. Nerf: Representing scenes as neural radiance fields for view synthesis. In *ECCV*, 2020.

Takeru Miyato, Bernhard Jaeger, Max Welling, and Andreas Geiger. Gta: A geometry-aware attention mechanism for multi-view transformers. In *ICLR*, 2024.

Thomas Müller, Alex Evans, Christoph Schied, and Alexander Keller. Instant neural graphics primitives with a multiresolution hash encoding. *ACM Trans. Graph.*, 41(4):102:1–102:15, July 2022.

T. Neff, P. Stadlbauer, M. Parger, A. Kurz, J. H. Mueller, C. R. A. Chaitanya, A. Kaplanyan, and M. Steinberger. Donerf: Towards real-time rendering of compact neural radiance fields using depth oracle networks. *Computer Graphics Forum*, 40:45–59, 2021.

Albert Pumarola, Enric Corona, Gerard Pons-Moll, and Francesc Moreno-Noguer. D-nerf: Neural radiance fields for dynamic scenes. *arXiv preprint arXiv:2011.13961*, 2020.

Christian Reiser, Songyou Peng, Yiyi Liao, and Andreas Geiger. Kilonerf: Speeding up neural radiance fields with thousands of tiny mlps, 2021.

Mehdi S. M. Sajjadi, Henning Meyer, Etienne Pot, Urs Bergmann, Klaus Greff, Noha Radwan, Suhani Vora, Mario Lucic, Daniel Duckworth, Alexey Dosovitskiy, Jakob Uszkoreit, Thomas Funkhouser, and Andrea Tagliasacchi. Scene Representation Transformer: Geometry-Free Novel View Synthesis Through Set-Latent Scene Representations. *CVPR*, 2022.

Vincent Sitzmann, Justus Thies, Felix Heide, Matthias Nießner, Gordon Wetzstein, and Michael Zollhöfer. Deepvoxels: Learning persistent 3d feature embeddings. In *Proc. CVPR*, 2019.

Shuyang Sun, Xiaoyu Yue, Song Bai, and Philip Torr. Visual parser: Representing part-whole hierarchies with transformers, 2022.

Stanislaw Szymanowicz, Christian Rupprecht, and Andrea Vedaldi. Splatter image: Ultra-fast single-view 3d reconstruction. In *CVPR*, 2024.

M. Tatarchenko, A. Dosovitskiy, and T. Brox. Octree generating networks: Efficient convolutional architectures for high-resolution 3d outputs. In *ICCV*, 2017.

Fengrui Tian, Shaoyi Du, and Yueqi Duan. MonoNeRF: Learning a generalizable dynamic radiance field from monocular videos. In *ICCV*, October 2023.

Qijian Tian, Xin Tan, Yuan Xie, and Lizhuang Ma. Drivingforward: Feed-forward 3d gaussian splatting for driving scene reconstruction from flexible surround-view input, 2024.

Adam Tonderski, Carl Lindström, Georg Hess, William Ljungbergh, Lennart Svensson, and Christoffer Petersson. Neurad: Neural rendering for autonomous driving. *arXiv preprint arXiv:2311.15260*, 2023.

Liao Wang, Jiakai Zhang, Xinhang Liu, Fuqiang Zhao, Yanshun Zhang, Yingliang Zhang, Minye Wu, Jingyi Yu, and Lan Xu. Fourier plenoctrees for dynamic radiance field rendering in real-time. In *CVPR*, pp. 13524–13534, 2022.

Qianqian Wang, Zhicheng Wang, Kyle Genova, Pratul Srinivasan, Howard Zhou, Jonathan T. Barron, Ricardo Martin-Brualla, Noah Snavely, and Thomas Funkhouser. Ibrnet: Learning multi-view image-based rendering. In *CVPR*, 2021a.

Wenhai Wang, Enze Xie, Xiang Li, Deng-Ping Fan, Kaitao Song, Ding Liang, Tong Lu, Ping Luo, and Ling Shao. Pyramid vision transformer: A versatile backbone for dense prediction without convolutions, 2021b.

Maximum Wilder-Smith, Vaishakh Patil, and Marco Hutter. Radiance fields for robotic teleoperation, 2024.

Zhuofan Xia, Xuran Pan, Shiji Song, Li Erran Li, and Gao Huang. Vision transformer with deformable attention, 2022.

Haozhe Xie, Hongxun Yao, Xiaoshuai Sun, Shangchen Zhou, and Shengping Zhang. Pix2vox: Context-aware 3d reconstruction from single and multi-view images. In *ICCV*, 2019.

Haofei Xu, Anpei Chen, Yuedong Chen, Christos Sakaridis, Yulun Zhang, Marc Pollefeys, Andreas Geiger, and Fisher Yu. Murf: Multi-baseline radiance fields. In *CVPR*, 2024.

Zhiwen Yan, Weng Fei Low, Yu Chen, and Gim Hee Lee. Multi-scale 3d gaussian splatting for anti-aliased rendering, 2024.

Jianwei Yang, Chunyuan Li, Pengchuan Zhang, Xiyang Dai, Bin Xiao, Lu Yuan, and Jianfeng Gao. Focal self-attention for local-global interactions in vision transformers, 2021.

Yuanwang Yang, Qiao Feng, Yu-Kun Lai, and Kun Li. R2human: Real-time 3d human appearance rendering from a single image, 2024.

Yao Yao, Zixin Luo, Shiwei Li, Tian Fang, and Long Quan. Mvsnet: Depth inference for unstructured multi-view stereo. In *ECCV*, 2018.

Alex Yu, Ruilong Li, Matthew Tancik, Hao Li, Ren Ng, and Angjoo Kanazawa. PlenOctrees for real-time rendering of neural radiance fields. In *ICCV*, 2021a.

Alex Yu, Vickie Ye, Matthew Tancik, and Angjoo Kanazawa. pixelNeRF: Neural radiance fields from one or few images. In *CVPR*, 2021b.

Xiaoyu Yue, Shuyang Sun, Zhanghui Kuang, Meng Wei, Philip Torr, Wayne Zhang, and Dahua Lin. Vision transformer with progressive sampling, 2021.

Pengchuan Zhang, Xiyang Dai, Jianwei Yang, Bin Xiao, Lu Yuan, Lei Zhang, and Jianfeng Gao. Multi-scale vision longformer: A new vision transformer for high-resolution image encoding, 2021.

Richard Zhang, Phillip Isola, Alexei A Efros, Eli Shechtman, and Oliver Wang. The unreasonable effectiveness of deep features as a perceptual metric. In *CVPR*, 2018.

Shunyuan Zheng, Boyao Zhou, Ruizhi Shao, Boning Liu, Shengping Zhang, Liqiang Nie, and Yebin Liu. Gps-gaussian: Generalizable pixel-wise 3d gaussian splatting for real-time human novel view synthesis. In *CVPR*, 2024.

Tinghui Zhou, Richard Tucker, John Flynn, Graham Fyffe, and Noah Snavely. Stereo magnification: Learning view synthesis using multiplane images, 2018.

Xizhou Zhu, Weijie Su, Lewei Lu, Bin Li, Xiaogang Wang, and Jifeng Dai. Deformable detr: Deformable transformers for end-to-end object detection. *arXiv preprint arXiv:2010.04159*, 2020.

A   APPENDIX

A.1   PRELIMINARY

A.1.1   3D GAUSSIAN SPLATTING

3D Gaussian Splatting (Kerbl et al., 2023) represents a 3D scene as a set of explicit Gaussian primitives as follows:

$$\mathcal{G} = \{g_i | g_i = (\mu_i, \Sigma_i, \alpha_i, sh_i)\}_{i=i}^N \tag{10}$$

where each Gaussian has a center μ_i, a covariance Σ_i, an opacity α_i and spherical harmonics sh_i. Furthermore, given the scaling matrix S and rotation matrix R, we can calculate the covariance matrix:

$$\Sigma = RSS^T R^T \tag{11}$$

As explicit Gaussian primitives $\mathcal{G}$ can be rendered via an rasterization-based operation, such approach is much more cheaper in both time and memory compared to implicit neural fields (Mildenhall et al., 2020; Barron et al., 2021; Tian et al., 2023; Chen et al., 2021a; Garbin et al., 2021) or voxel-based representations(Sitzmann et al., 2019; Ji et al., 2017; Xie et al., 2019; Tatarchenko et al., 2017; Choy et al., 2016).

A.1.2   DEFORMABLE ATTENTION

Since the introduction of ViT (Dosovitskiy et al., 2021), numerous efficient attention mechanisms have been proposed to further enhance the scalability and reduce the complexity of ViT (Liu et al., 2021; Chen et al., 2021b; Wang et al., 2021b; Yang et al., 2021; Zhang et al., 2021; Dong et al., 2022; Jaegle et al., 2021; Sun et al., 2022; Zhu et al., 2020; Yue et al., 2021; Chen et al., 2021c). Among them, Deformable Attention Transformer (DAT) (Xia et al., 2022) stands out for its ability to effectively capture multi-scale features and adaptively focus on important regions while maintaining lightweight computational overheads. Therefore, we apply deformable attention in both the Score Hypernetworks $\mathcal{H}$ (equation 4) and Iterative Gaussian Refiner (IGR) (equation 8) in our PixelGaussian model. We elaborate equation 8 as an example.

Given Gaussian centers μ, corresponding queries $\mathcal{Q}$, feature maps $\mathcal{F} = \{F_i\}_{i=1}^N$ and camera parameters $\mathcal{C} = \{C_i\}_{i=1}^N$, we first project Gaussian centers to pixel coordinates to get reference points, denote as $\mathcal{R} = \{R_i\}_{i=1}^N$:

$$R_i = P(\mu, C_i), (i = 1, 2, ..., N) \tag{12}$$

where $P(\cdot)$ denotes projection operation. Next, for Gaussian queries $\mathcal{Q}$, we perform deformable sampling from feature maps $\mathcal{F}$ at reference points $\mathcal{R}$ using bilinear interpolation as follows:

$$\phi(F_i, (r_x, r_y)) = \sum_{(p_x, p_y)} g(r_x, p_x) \cdot g(r_y, p_y) \cdot F_i(p_x, p_y) \tag{13}$$

where $g(x, y) = max(0, 1 - |a - b|), (r_x, r_y), F_i$ denote reference point and feature map, respectively. Then we can update queries $\mathcal{Q}$ via attention:

$$\mathcal{Q} = \sum_{i=1}^N \alpha_i \cdot (W_i \cdot \phi(F_i, R_i)) \tag{14}$$

$$W_i = softmax(\mathcal{Q} \cdot \phi(F_i, R_i)^T) \tag{15}$$

where $\alpha_i, (i = 1, 2, ..., N)$ represents view weights as illustrated in equation 3. Following this paradigm, we incorporate deformable attention in the score hypernetworks $\mathcal{H}$ to generate context-aware thresholds, and in IGR blocks to further refine Gaussian representations using image features.

A.2   MORE IMPLEMENTATION DETAILS

Training Details. As mentioned in Section 4.1, our model is trained on 8 NVIDIA A6000 GPUs, The batch size for a single GPU is set to 4, where each batch contains a large-scale 3D scene with two reference views and four inference views. Detailed settings of image backbone to generate aggregated features $\mathcal{F}$, context-aware score hypernetworks $\mathcal{H}$ in Cascade Gaussian Adapter and

Table 5: Details of Gaussian Parameter Range.

Gaussian Parameters	Criterion
scaling $s \in \mathbb{R}^3$	$s_x, s_y, s_z \in [0.50, 15.00]$
rotation $r \in \mathbb{R}^4$	$||r|| = 1$
opacity $\alpha \in \mathbb{R}$	$\alpha \in [0, 1]$
harmonics $sh \in \mathbb{R}^C$	decaying coefficients

Table 6: Details of Training Settings

Config	Setting
optimizer	Adam
scheduler	Cosine Annealing
learning rate	2×10^{-4}
weight decay	1×10^{-4}

Table 7: Details of Network Architecture.

Block	Setting
CNN layers	[4, 4, 4]
CNN channels	[32, 64, 128]
Transformer layers	[2, 2, 2, 2, 2, 2]
Transformer channels	[128, 128, 128, 128, 128, 128]
Score HyperNetworks layers	[2, 2, 2]
Score HyperNetworks channels	[1, 1, 1]
IGR layers	[2, 2, 2]
IGR channels	[128, 128, 128]

Iterative Gaussian Refiner are illustrated in Table 7. For MLP-based networks in equation 6 and equation 9, they all follow criteria in Table 5 to ensure all Gaussian parameters within proper range.

Network Architecture. As illustrated in Table 7, the image backbone comprises a ResNet-based CNN (He et al., 2016) for feature extraction and a Swin Transformer (Liu et al., 2021) for multi-view attention. For context-aware score hypernetworks $\mathcal{H}$ in CGA, we employ $K = 3$ stages for adaptive Gaussian adaption. Then, we adopt $B = 3$ deformable attention blocks in IGR for Gaussian representation refinement.

A.3 MORE RESULTS

We provide more visualization comparisons of PixelGaussian and previous dominant pixel-wise methods (Charatan et al., 2023; Chen et al., 2024) on ACID (Liu et al.) and RealEstate10K (Zhou et al., 2018) benchmarks. Additionally, we provide visualizations of more score maps and Gaussian density maps from our PixelGaussian model. As shown in Figure 7 and Figure 8, PixelGaussian benefits from dynamic adaption of Gaussian distributions, resulting in superior reconstruction compared to previous pixel-wise methods.

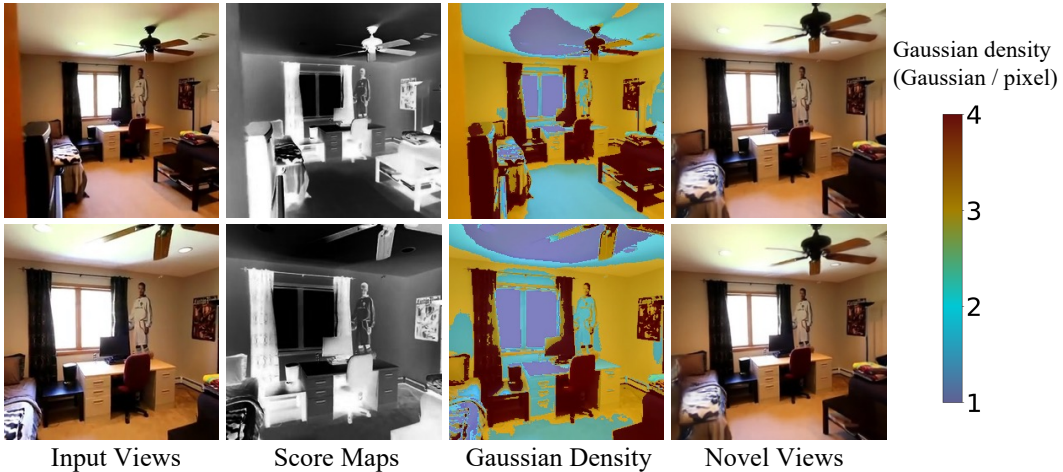| Input Views	Score Maps	Gaussian Density	Novel Views

Gaussian density (Gaussian / pixel)

Figure 7: Visualization of score maps and Gaussian distributions of Cascade Gaussian Adapter.

Figure 8: Visualization results on ACID (Liu et al.) and RealEstate10K (Zhou et al., 2018) benchmarks.